Metallurgy and materials
*Metalurgia e materiais*

# Development of core-shell nanocomposites containing iron oxide,silica and samarium for potential application in cancer treatments involving brachytherapy and magnetic hyperthermia

http://dx.doi.org/10.1590/0370-44672022760049

**Gabriela Veloso**[1,3]
https://orcid.org/0000-0001-8417-9033
**Roberta Ferreira**[1,4]
https://orcid.org/0000-0002-8934-2909
**Wanderley Roberto**[2,5]
https://orcid.org/0000-0003-1732-6317
**Sidney Nicodemos da Silva**[2,6]
https://orcid.org/0000-0002-4431-6651

[1]Centro Federal de Educação Tecnológica de Minas Gerais - CEFET-MG, Departamento de Engenharia de Materiais, Belo Horizonte – Minas Gerais - Brasil.

[2]Centro Federal de Educação Tecnológica de Minas Gerais - CEFET-MG, Departamento de Física, Belo Horizonte – Minas Gerais - Brasil.

E-mails: [3]gabrielaveloso.engmateriais@gmail.com, [4]robertavia@gmail.com, [5]wanderley@cefetmg.br, [6]sidneynicodemos@yahoo.com.br

## Abstract

Nanocomposites formed of natural-origin iron oxide nanoparticles (magnetite and maghemite, $Fe_3O_4$ and $\gamma$-$Fe_2O_3$, respectively) were processed using the sol-gel process into core-shell structures containing silica and samarium to investigate their potential for applications in cancer treatments combining hyperthermia and brachytherapy. Mössbauer characterization showed that the iron oxides contained 64% magnetite, 18% hematite, 12% maghemite, and exhibit superparamagnetic behavior at room temperature. Transmission electron microscopy determined that the iron oxide particles were smaller than 15 nm, while magnetization was measured at 5 emu/g. Fourier transform infrared indicated the material was formed of Si-O-Si and Fe-O-Si bonds, while X-ray diffraction showed bands of amorphous silica from 5° to 23° and bands of iron oxide phases. X-ray fluorescence indicated 5.17% of incorporated samarium. The nanocomposite suspensions were subjected to an alternating magnetic field and the resulting heat dissipation was measured, falling within the ideal range for hyperthermia applications. Theoretical dosimetric calculation determined significant radioactive activity of $1.68x10^{-8}$ $MBq.mg^{-1}.\Phi^{-1}$ after 24h decay time for $^{153}Sm$. The characteristics and behavior of these nanocomposites indicate that they may offer promise in applications involving hyperthermia for cancer treatment and a more accessible source for brachytherapy materials.

**Keywords:** nanocomposites, sol-gel, iron oxide, samarium, silica, brachytherapy/magnetic hyperthermia, cancer.

## 1. Introduction

Cancer still causes high mortality rates worldwide, despite research efforts and the development of new drugs and treatments by the pharmaceutical industry. The most common cancer treatments are currently surgery, radiotherapy, and chemotherapy. Various factors influence the success of treatment, including cancer classification, staging, volume, location, and metastasis. The disadvantages and limitations of conventional treatments have driven investments in research to find more assertive and less invasive combined treatments (WHO, 2020; IARC, 2020; INCA, 2021).

Brachytherapy is an efficient traditional cancer treatment. While conventional radiotherapy applies radiation from outside the body to the area where the tumor is located, potentially affecting healthy cells, brachytherapy applies radiation within the body. An implant containing radioactive material is introduced into the region where the tumor is located, releasing a high dose of local radiation to eliminate tumor cells while preserving the surrounding healthy tissue. This treatment decreases the risk of common side effects such as fatigue, hair loss, and skin redness, dryness, and irritation (Cember & Johnson, 2009).

The radioactive implant material (known as a seed) currently used in clinical applications is made of titanium filled with iodine-125 ($^{125}I$). Some important limiting factors in this technique are the efficiency of the chosen radionuclide, the number of seeds required, the size and dispersion of seeds in the body, as well their permanence within in the tumor. Other radionuclides may offer better conditions for brachytherapy. The rare earth element isotope samarium-152 ($^{152}Sm$) incorporated into a ceramic matrix synthesized using the sol-gel process offers such potential and can produce seeds of suitable sizes (Chilton *et al*. 1984; Cember, 1987; Roberto *et al*., 2003; Mathari *et al*., 2004). A recent study indicated that another rare earth element, holmium-166, may also be useful for brachytherapy within a ceramic matrix (Delpino *et al*., 2021).

Cancer therapy involving magnetic hyperthermia (MH) is based on the observation that tumor cells are less resistant to temperature increases than healthy cells; MH involves dispersing magnetic particles throughout the diseased tissue and applying an alternating magnetic field of sufficient intensity and frequency to heat these particles. The tumor cells consequently lyse at approximately 41–42 °C, with no damage to the healthy cells. This type of treatment is less destructive to the plasma membrane than conventional thermotherapy (41–45 °C), which can damage DNA, denature proteins, alter the pH in the local microenvironment, and induce apoptosis in the tumor cells (Ferreira, 2009). Magnetic hyperthermia can be utilized alone or in combination with conventional therapies. Various materials are currently being investigated for use in MH: metals, metal oxides, metal alloys, porous oxides, and polymers (Dönmez *et al*., 2019).

The iron oxides magnetite ($Fe_3O_4$) and maghemite ($\gamma$-$Fe_2O_3$) have been widely investigated for such applications; they dissipate heat in response to an alternating magnetic field, and consequently offer significant potential in MH (Pareta & Sirivisoot, 2012; Gilchrist *et al*., 1957). An additional and important advantage of iron oxide particles is that when they degrade within the body they release iron ions that can be incorporated into the hemoglobin or utilized by conventional organic cycles, and are therefore biocompatible. But because these particles are prone to aggregation and sedimentation, it is important to surround magnetic nanoparticles with a non-magnetic layer for in vivo applications (Mahmoudi *et al*., 2011).

This article describes the preparation and characteristics of silica particles containing iron oxide and samarium (Si-Mag-Sm) for potential application in cancer treatments combining hyperthermia and brachytherapy.

## 2. Materials and methods

### 2.1 Preparation of iron oxide samples

Natural iron oxide was obtained from ilmenite ($FeTiO_3$) ore, a byproduct of titanium ($TiO_2$) extraction activities (provided by Phosther Inovações, Santa Luzia, Brazil). The material underwent comminution in a ball mill to remove impurities and was sieved at 400 mesh.

### 2.2 Preparation of silica samples containing iron oxide and samarium

Two samples were produced in this study: silica containing iron oxide (Si-Mag), and silica containing iron oxide and samarium (Si-Mag-Sm). The samples were prepared using the modified Stöber method (Ebelmen, 1846; Wright & Sommerdijk, 2018; Stöber *et al*., 1968).

To synthesize the Si-Mag-Sm particles, 640 mL ethanol (EXODO), 160 mL distilled water, 20 mL ammonium hydroxide (NEON), 4 mL tetraethyl orthosilicate (TEOS, Sigma Aldrich), 0.16 g iron oxide, and 0.16 g samarium nitrate hexahydrate (Sigma Aldrich) were added to a 1 L polypropylene beaker. The resulting suspension was subjected to sonication for 20 minutes to better disperse the particles, and then stirred using a magnetic stirrer (IKA C MAG HS 7 model) for 24 hours at room temperature (RT) after sealing the beaker with PVC film. After 24 h, the particles were washed with distilled water and collected with a magnet (neodymium-iron-boron magnet plate measuring 10 cm x 10 cm x 2 cm) and transferred to a petri dish. The samples were left in a humid atmosphere for 24 h and then frozen and freeze-dried for 24 h. The Si-Mag sample was obtained using the same procedure, without the addition of samarium nitrate.

### 2.3 Theoretical neutron activation analysis method

Neutron activation can be used to transform $^{152}Sm$ into $^{153}Sm$. In this process, a sample containing $^{152}Sm$ atoms is bombarded with neutrons, and activation occurs via the nuclear reaction $n + {}^{152}Sm \rightarrow {}^{153}Sm + \gamma$ accompanied by the decay $^{153}Sm \rightarrow \gamma + \beta + X$.

In order to simulate the radioactive activity of each chemical element

in the sample as a function of its chemical concentration, theoretical neutron activation analysis was calculated. The ideal activity of chemical elements when subjected to a neutron beam can be obtained from Equation 1 (Chilton *et al.*, 1984; Cember, 1987; Roberto *et al.*, 2003; Mathari *et al.*, 2004):

$$A(t) = 0.6025 \cdot \frac{\omega.ma}{A} \left(\sigma_{ep}\varphi_{ep} + \sigma_{th}\varphi_{th}\right) \cdot \left(1-e^{-\lambda.t}\right) \cdot e^{-\lambda.\delta} \qquad (1)$$

In this expression, ω represents the concentration of the element in the sample (%), m is the mass of the material to be activated (g), a is the isotopic abundance (%), A is the atomic mass (g) of the element, $\varphi_{th}$ and $\varphi_{ep}$ represent the thermal and epithermal fluxes ($n.cm^{-2}.s^{-1}$), respectively, $\sigma_{th}$ and $\sigma_{ep}$ represent the shock sections for thermal and epithermal neutrons (barns), respectively, λ is the disintegration constant expressed in $s^{-1}$, t is the time (s) the material is exposed to the stream of neutrons, and δ is the decay time after activation (s).

## 2.4 Characterization of the samples

### 2.4.1 Characterization of iron oxide samples

Scanning electron microscopy (SEM) imagery was obtained using a Tescan Vega microscope, and a secondary electron detector at 20 mV was used to obtain high-resolution images. The SEM images were obtained at Phosther Inovações, and TEM was conducted at the Leibniz Institute for New Materials (INM) in Saarbrücken, Germany. Micrographs of the samples were acquired with a Tecnai G2-20 Super-Twin FEI microscope at 200 kV. Several drops of the nanoparticle suspension were deposited on the microscope grid and images were obtained after solvent evaporation.

The samples were analyzed using X-ray diffraction (XRD) at the CEFET-MG Characterization and Microscopy Laboratory using a Shimadzu XRD-7000 diffractometer operating under the following conditions: CuKα radiation (35 KV/40 mA), goniometer speed 0.02° at 2θ per step, with standard counting time per step and collected from 5° to 80° at 2θ. The data were compared with standards contained in the PDF2 database (International Center for Diffraction Data, ICDD, 2003) in X-Powder Ver. 2004.04.70 software, and confirmed against examples in literature.

Mössbauer spectroscopy analysis was conducted on $^{57}Fe$ in a spectrometer at the Center for the Development of Nuclear Technology (CDTN) at the Federal University of Minas Gerais (UFMG), with constant acceleration and $^{57}Co$ source in the Rh matrix maintained at RT using transmission geometry. The Mössbauer system at CDTN uses a transducer controlled by a linear function control unit and proportional counter-type radiation detectors with a gas chamber containing 97% krypton and 3% $CO_2$ at 1 atm pressure. Spectra were obtained at RT and quantitative analyses of the data conducted using the Normos program; isomeric shifts were standardized according to natural Fe (α-Fe) (Ferreira, 2009).

The magnetic properties of the samples were also evaluated at CDTN using a LakeShore model 7404 vibrating sample magnetometer. Hysteresis curves were subsequently obtained from these measurements, providing data about the magnetic properties of the analyzed material.

Heat dissipation was measured using EASYHEAT equipment (Ambrell). The samples were suspended in water, placed inside plastic tubes, and positioned in the middle of an induction coil with a frequency of 356 kHz. An alternating magnetic field (AMF) was applied initially for 30 s, and the temperature increase after AMF exposure was measured with a digital thermometer (WT-1). The procedure was repeated after increasing the exposure time in increments of 30 s.

### 2.4.2 Characterization of silica particles containing iron oxide and samarium

The chemical composition of the Si-Mag and Si-Mag-Sm samples was determined with X-ray fluorescence using a Shimadzu EDX-720 device. The analyses were performed under vacuum.

The samples were characterized using XRD at the CEFET-MG Characterization and Microscopy Laboratory using a Shimadzu XRD-7000 diffractometer operating under the following conditions: CuKα radiation (35 KV/40 mA), goniometer speed 0.02° at 2θ per step, with standard counting time per step and collected from 5° to 80° at 2θ. The data were compared with standards contained in the PDF2 database (International Center for Diffraction Data, ICDD, 2003) in X-Powder Ver. 2004.04.70 software, and supported by examples found in literature.

The chemical composition of the samples was also analyzed via Fourier transform infrared spectroscopy (FTIR) using a Shimadzu IR Prestige-21 device operated in ATR mode in the 4000 $cm^{-1}$ to 400 $cm^{-1}$ wavenumber range, with resolution of 4 $cm^{-1}$.

## 3. Results and discussion

### 3.1 Iron oxide particles

The SEM imaging revealed aggregation of the iron oxide particles, combining up to 50 reactive atoms or molecules (Figure 1). Nanoparticles form agglomerates with weak physical interactions that are easily dispersed with ultrasound; in other words, the particles in the form of colloids are micrometric aggregates due to weak electrostatic interactions. The TEM images (Figure 1) also indicate that the particles are smaller than 15 nm, a useful size for biomedical applications, primarily because this controllable size permits interaction with cells (10-100 μm), viruses (20-450 nm), proteins (5-50 nm), and genes (2 nm thick, 10–100 nm long). Furthermore, the sample's magnetic properties are of great interest since they allow manipulation by an external magnetic field gradient (Ferreira, 2009). The silica coating (core-shell) is intended to inhibit aggregation of the nanoparticles or formation of agglomerates with weak electrostatic interactions between the particles, potentially providing electrostatic repulsion of the synthesized particles (steric impediment).

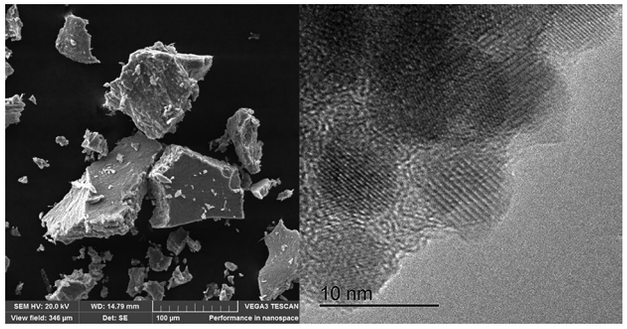


Figure 1 - SEM (left) and TEM (right) images of natural iron oxide.

Figure 2 shows the diffractogram of natural and synthetic magnetite (produced by a coprecipitation route (Ferreira, 2010). The synthetic magnetite was produced by Lana (2018) for comparison with natural magnetite obtained from mining activity; both studies use the same natural magnetite to compare chemical composition, phases present, magnetization, dispersion, and biocompatibility.

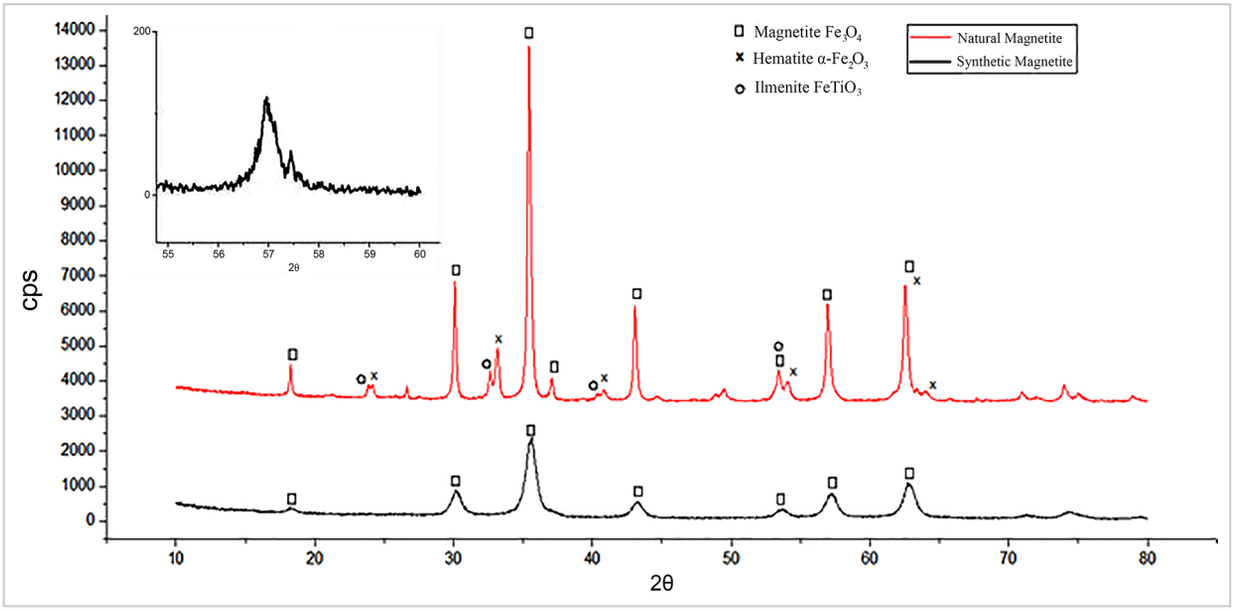


Figure 2 - XRD of the natural and synthetic magnetite samples; insert details the peaks of the magnetite and maghemite phases.

In the diffractogram at RT, a peak appeared at 57°, corresponding to the plane (511); the region between 55° and 60° was selected. Two separate peaks are visible at 57° and 57.5°, referring to the magnetite and maghemite phases, respectively. The ilmenite present in this sample is considered an impurity, since the sample was obtained from industrial titanium mining. A primary treatment method using low-field magnetic separation was used to eliminate some of the residual titanium oxide in the sample received.

The Mössbauer spectra obtained are shown in Figure 3 and Table 1. The synthesized sample was produced by the coprecipitation route of Fe (II) and Fe (III) ions with ammonium hydroxide in an inert nitrogen atmosphere, as described by Ferreira (2009).

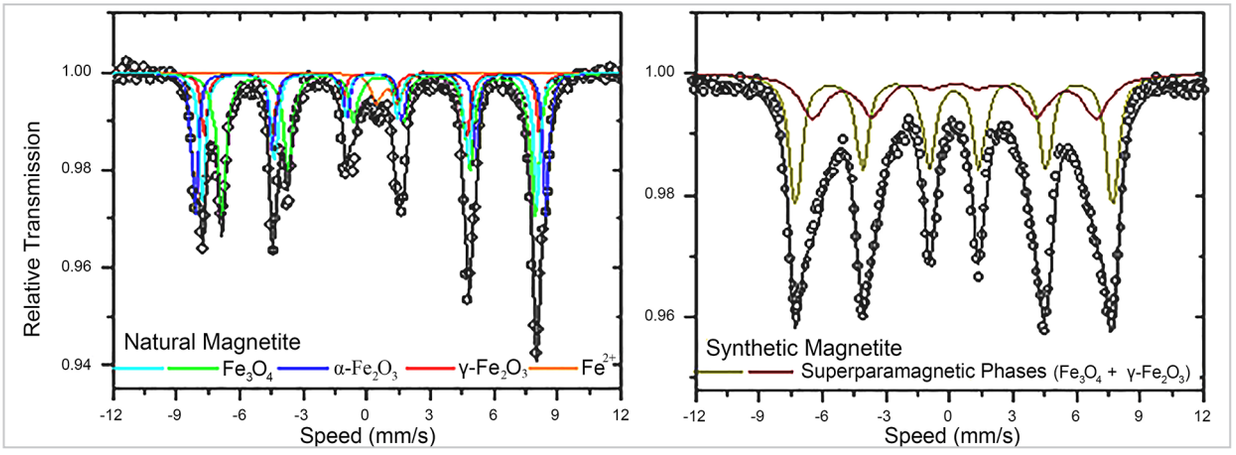


Figure 3 - Result of the $^{57}$Fe Mössbauer spectrum for the iron oxide (natural magnetite) sample obtained at RT.

Mössbauer spectroscopy analysis showed that the iron oxide (natural magnetite) sample presents a spectrum with narrow lines (or peaks) compared to other synthetic magnetite samples in literature (Ferreira, 2009), which exhibit spectra with broad peaks; both are characteristic of iron oxide mixtures with superparamagnetic behavior at RT.

Table 1 - Hyperfine parameters of the Mössbauer spectra for 57Fe obtained at RT.

| Sample | Phase | δ ± 0.05 (mm/s) | Deq ± 0.05 (mm/s) | $B_{HF}$ ± 0.5 (T) | Relative Area ±(1%) |
|---|---|---|---|---|---|
| Natural Magnetite | $\alpha$-$Fe_2O_3$ | 0.37 | -0.17 | 51.,4 | 18 |
| | $Fe_3O_4$ | 0.65 | 0.01 | 45.8 | 43 |
| | | 0.23 | -0.02 | 48.9 | 21 |
| | $\gamma$-$Fe_2O_3$ (*) | 0.30 | 0.09 | 49.16 | 12 |
| | $Fe_{1-x}O$ | 1.05 | 0.98 | - | 6 |

(*) Superparamagnetic behavior at RT.

The following oxides were identified in the natural sample: magnetite ($Fe_3O_4$) majority phase (64%), maghemite ($\gamma$-$Fe_2O_3$), hematite ($\alpha$-$Fe_2O_3$) minority phases (12% and 18%, respectively), and traces of other oxides (6%). The technique provides values for the isomeric shift of the phases relative to αFe, provided by δ. Values for quadrupole unfolding (D) and hyperfine magnetic field (Bhf) were also obtained.

The magnetization measurements of the natural material are presented in Figure 4 and compared with those for synthetic magnetite.

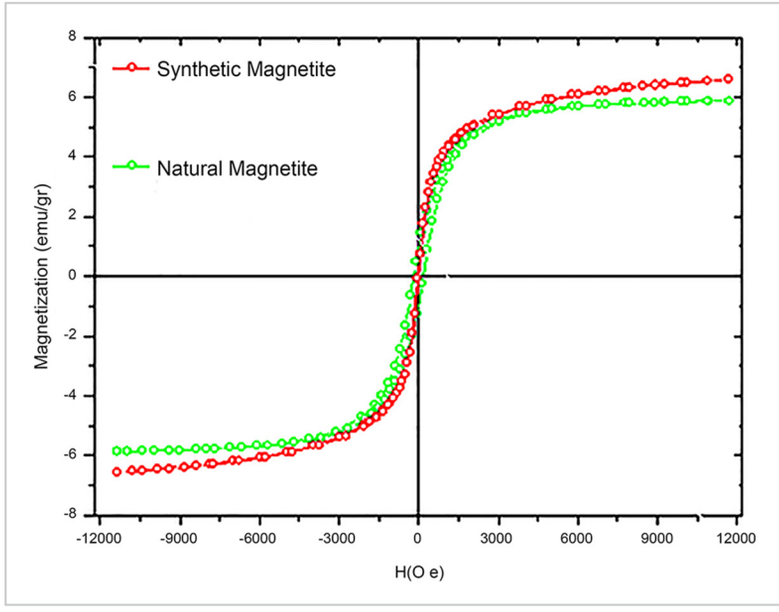


Figure 4 - Magnetization measurements of natural and synthetic magnetite.

The saturation magnetization values (σs) for both samples shown in Figure 4 are lower than those for standard non-nanostructured magnetite, in the order of 92 emu/g. However, the low saturation magnetization of these natural or synthetic magnetite samples may be associated with the ultrafine particles present. Because of the surface area of these particles, the magnetic moments do not remain fully aligned, and as a result the higher surface area-volume ratio (from the smaller particle) leads to greater contribution of unaligned moments and lower magnetization. For natural magnetite, the low σs is due to the surface effect and presence of other non-magnetic oxides, which were also detected in XRD (shown in Figure 2) and Mössbauer spectroscopy. The high coercivity value in natural magnetite can be attributed to the portion of particles approximately 15–25 nm in size, while the coercivity value for synthetic magnetite (close to zero) may be associated with the slightly smaller particle size (around 10 nm). The results show low hysteresis loss in both samples and very similar behavior when exposed to alternating electromagnetic fields. Natural magnetite appears to have low coercivity, with a small area in the hysteresis cycle (see Figure 4; low energy expenditure to change magnetization or reduced intensity of the external field was applied to magnetize the material) and remaining magnetization of less than 1.0 emu/g. The high magnetic permeability (μ) observed at the start of the magnetization cycle confirms the superparamagnetic properties of these materials.

The semi-quantitative results of chemical analysis using X-ray fluorescence spectroscopy (XRF) are presented in Table 2.

Table 2 - Metal quantification of natural magnetite, using XRF.

| Quantitative Result | | |
|---|---|---|
| **Analyte** | **Result (%)** | **Standard Deviation** |
| **Fe** | 91.437 | [0.205] |
| **Ti** | 5.244 | [0.056] |
| **Mn** | 0.880 | [0.017] |
| **Ca** | 0.865 | [0.021] |
| **P** | 0.648 | [0.116] |
| **S** | 0.319 | [0.046] |
| **V** | 0.302 | [0.021] |
| **Zn** | 0.116 | [0.013] |
| **Cr** | 0.069 | [0.011] |
| **Nb** | 0.050 | [0.006] |
| **Zr** | 0.036 | [0.006] |
| **Sr** | 0.033 | [0.006] |

The Si-Mag and Si-Mag-Sm samples were analyzed using XRF and the elementary percentage values were collected; Table 3 presents the resulting theoretical and experimental elemental proportions of Fe, Si, and Sm in the samples.

Note that the natural magnetite sample contains other elements in addition to iron oxides such as titanium and manganese, likely a result of the mining process. The natural magnetite sample contains over 91% iron. Since this is a semi-quantitative analysis, the other elements found can be considered trace amounts or interferences of the technique.

## 3.2 Si-Mag and Si-Mag-Sm samples

Transmission electron microscopy of the Si-Mag and Si-Mag-Sm samples revealed roughly spherical particles with a regular average size. The maghemite nanoparticles were encapsulated with a homogeneous silica shell. The average diameter of the silica-coated magnetic nanoparticles was 43 nm, compared to 39 nm for the Si-Mag and Si-Mag-Sm samples (Figure 5).

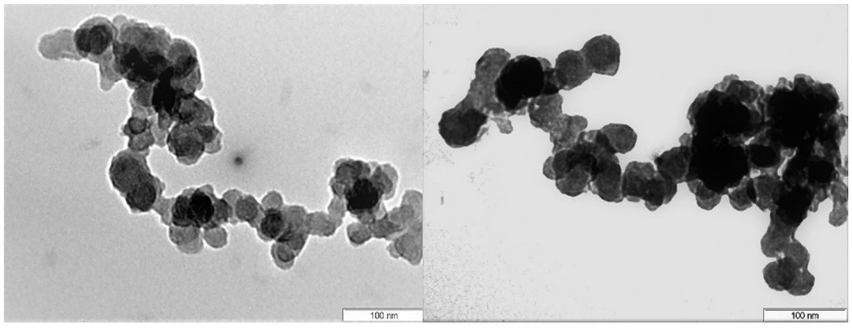


Figure 5 - TEM images of the Si-Mag (left) and Si-Mag-Sm (right) nanoparticles.

The samples of Si-Mag and Si-Mag-Sm were analyzed using XRF and the percent elemental values were collected. The experimental elemental ratios of Fe, Si, and Sm obtained from the samples are shown below in Table 3.

Table 3 - Experimental elemental compositions obtained using XRF analysis.

| Element | Si-Mag (%) | Si-Mag-Sm (%) |
|---|---|---|
| Fe | 88.775 | 50.556 |
| Si | 4.120 | 40.652 |
| Sm | - | 5.169 |
| Ti | 3.617 | 2.204 |
| Mn | 0.720 | 0.343 |
| V | - | 0.140 |
| Al | - | 0.936 |
| Cr, Zr, Bi, Nb, Ba | 2.768 | - |
| **Total** | **100** | **100** |

The elemental analysis using XRF indicated that silica containing samarium and iron oxide was obtained. Some impurities from the iron oxide sample were also incorporated into the system. The Si-Mag sample contained approximately one tenth the quantity of silica in the Si-Mag-Sm sample, indicating that samarium seems to favor the production of core-shell structures in association with silica. When samarium nitrate was present, less iron oxide was incorporated (dropping from 89% to 51%), indicating that samarium seems to disfavor the incorporation of iron oxide into the coating (Dönmez *et al.*, 2019; Mahmoudi, 2011). This behavior requires further investigation.

X-ray diffractograms were obtained for the Si-Mag and Si-Mag-Sm samples, and are presented in Figure 6.

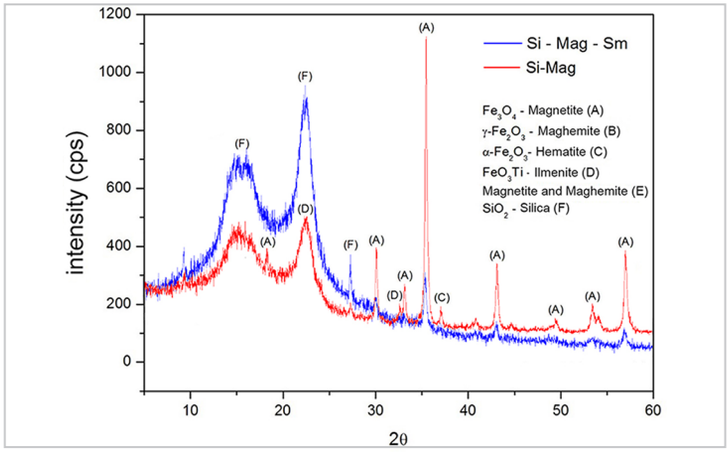


Figure 6 - X-ray diffractogram for the Si-Mag and Si-Mag-Sm samples.

The X-ray diffractogram for the Si-Mag sample exhibited peaks from 5° to 23° and at 18°, 30°, 35.5°, 43°, 53°, and 57°. The XRD analysis was compared with tabulated standards for magnetite ($Fe_3O_4$) (PDF 19-0629), maghemite ($\gamma$-$Fe_2O_3$), (PDF 39-1346) and hematite ($\alpha$-$Fe_2O_3$) (PDF 87-1166) obtained from the PDF2 database. The diffractogram exhibits broad bands from 5° to 23° that refer to amorphous silica. Roberto *et al.*5 also attributed this low intensity of crystalline peaks to the predominant amorphous characteristic of their sample obtained using the sol-gel process.

The peaks at 18°, 30°, 35.5°, 43°, 53°, and 57° indicate the presence of magnetite, with 30.3°and 43.5° referring to the maghemite phase. The peak at 33° indicates the presence of hematite, while the peaks at 23.9° and 32.5° confirm the presence of ilmenite, a natural oxide of iron and titanium ($FeTiO_3$) from titanium mining. The diffractogram of the Si-Mag sample shows the formation of silica and incorporation of the iron oxide particles.

The X-ray diffractogram for the Si-Mag-Sm sample exhibited peaks from 5° to 23° and at 27.7°, 35.5°, 43°, and 57°. Broad bands are seen from 5° to 23° that refer to amorphous silica, as in the previous sample. The percentage of iron oxide in the sample decreased when samarium nitrate was incorporated into the complex, corroborated by the XRF technique; this behavior requires additional investigation. The samarium peaks expected between 13° and 31° were not observed, indicating that these may be convoluted by the amorphous halo, since a drop in the crystallinity of the sample was observed (seen in the formation of the characteristic bands of silica). The diffractogram obtained by Deepa *et al.* (2016) showed that borate glasses doped with samarium oxide exhibit a broad diffusion band at lower scattering angles, indicating the presence of a long-range structural disorder, characteristic of an amorphous nature; another reason for the absence of the expected peaks. Furthermore, a considerable decrease in the intensities of the magnetite peaks was observed in the sample, accompanied by the subsequent appearance of the peak attributed to maghemite, which may be related to an oxidative process that occurred during coating. This may also be related to the addition of samarium nitrate to the synthesis, indicating its influence on the iron oxides.

Infrared spectroscopy (FTIR) was used to characterize the Si-Mag and Si-Mag-Sm samples; the spectra obtained are shown in Figure 7.

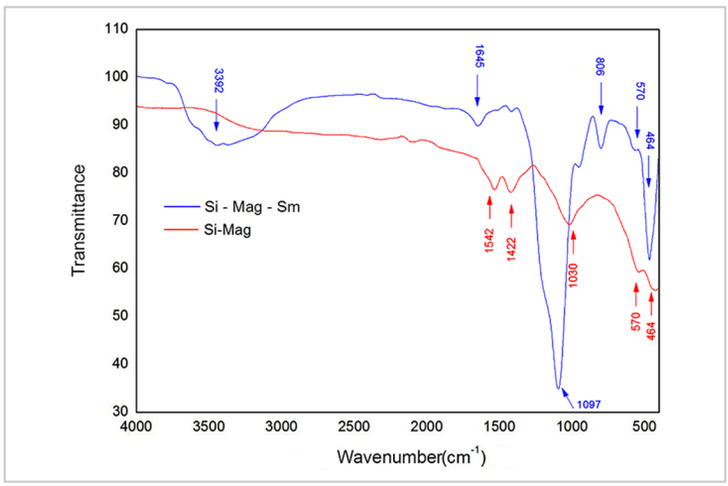


Figure 7 - FTIR spectra for the Si-Mag and Si-Mag-Sm samples.

The FTIR spectrum obtained for the silica sample containing iron oxides shows bands at 1542, 1422, 1030, 570 and 464 $cm^{-1}$. The last two bands confirm the presence of iron oxide in the sample, since they are associated with the Fe-O bonds; the other bands are associated with the presence of the silica particles formed. The silica is adsorbed onto the magnetite surface via Fe-O-Si bonds. Incorporation of the iron oxide into the silica particle can be confirmed by the presence of the band at 570 $cm^{-1}$ (Ferreira, 2009). Such a band can be attributed to the vibration of the Fe-O bond in the $Fe_3O_4$ crystal structure. The 1030 $cm^{-1}$ vibrational mode is part of the glassy network of the material formed by Si-O-Si bonds (Hwa, 1998), confirming that silica was formed from its TEOS precursor. The bands in the 1600–1400 $cm^{-1}$ range are related to the -OH functional group present on the surface of silica (OH) particles (Rubio, 1998; Moreira & Peçanha, 2017).

The FTIR spectrum obtained for the silica sample containing magnetic and samarium particles exhibits bands at 3392, 1645, 1097, 806, 580, and 464 $cm^{-1}$. The 464 $cm^{-1}$ band assigned to the Fe-O bond confirms the presence of iron oxide in the structure of the obtained silica particle. A reduction was observed in the 570 $cm^{-1}$ band, which like the 464 $cm^{-1}$ band, also appears in the spectrum of the Si-Mag sample. The band at 570 $cm^{-1}$, as in the previous sample, is attributed to the Fe-O-Si bond. This reduction of the two bands can be attributed to the reduced concentration of iron particles incorporated into the sample due to the addition of samarium, and can be confirmed by the XRF results.

The 1097 $cm^{-1}$ band is attributed to the Si-O-Si bond, as described for the previous sample, which also proves that silica was formed in this sample. In this region (approximately the 1033 $cm^{-1}$ range) the vibration referring to $Sm^{+3}$ would also be expected (Vratny & Kokalas, 1962; Deepa & Priya, 2016), but the higher proportion of silica present may interfere with the Si-O-Si bond band in the samarium. The broad band at 3392 $cm^{-1}$ is attributed to the stretching of -OH groups and the band at 1645 $cm^{-1}$ is attributed to the deformation of the H-O-H bond, suggesting the existence of adsorbed water on the surface of the particles (Chanéac *et al.*, 1996).

Table 4 presents the results for the initial and final activity calculations (after 24 h) for the elements with experimental elemental percentages displayed in Table 3.

Table 4 - Initial and final activity calculations for the elements in the Si-Mag-Sm sample, determined by XRF.

| Parent Element | a (%) | $\sigma_{th}$ barns | $\sigma_{ep}$ barns | Daughter Element | Half-Life | A* $MBq.mg^{-1}.\varphi^{-1}$ | A‡δ $MBq.mg^{-1}.\varphi^{-1}$ |
|---|---|---|---|---|---|---|---|
| $^{54}Fe$ | 5.8 | 2.252 | 1.32 | $^{55}Fe$ | 2.73 a | $1.15x10^{-9}$ | $1.14x10^{-9}$ |
| $^{58}Fe$ | 0.28 | 0.149 | 1.23 | $^{59}Fe$ | 44.503 d | $2.06x10^{-11}$ | $2,03x10^{-11}$ |
| $^{56}Ti$ | 5.4 | 0.178 | 0.14 | $^{57}Ti$ | 5.76 min | $4.45x10^{-10}$ | $4.00x10^{-85}$ |
| $^{144}Sm$ | 3.1 | 1.63 | 1.902 | $^{145}Sm$ | 430 d | $2.26x10^{-2}$ | $2.23x10^{-12}$ |
| $^{152}Sm$ | 26.7 | 206.2 | 2764.4 | $^{153}Sm$ | 46.284 h | $2.40x10^{-8}$ | $1.68x10^{-8}$ |
| $^{154}Sm$ | 22.7 | 8.325 | 8.93 | $^{155}Sm$ | 22.3 min | $6.41x10^{-9}$ | $4.67x10^{-28}$ |
| $^{30}Si$ | 3.1 | 0.1075 | 0.708 | $^{31}Si$ | 157.3 min | $4.97x10^{-8}$ | $8.75x10^{-11}$ |
| $^{55}Mn$ | 100 | 13.41 | 13.3 | $^{56}Mn$ | 2.579 h | $2.32x10^{-8}$ | $3.70x10^{-11}$ |
| $^{51}V$ | 0.14 | 4.9 | 4.8 | $^{52}V$ | 3.743 min | $1.22x10^{-8}$ | $3.28x10^{-124}$ |
| $^{27}Al$ | 100 | 0.234 | 0.232 | $^{28}Al$ | 2.241 min | $8.38x10^{-17}$ | $4.78x10^{-210}$ |

* Irradiation time t=1h. ‡ Decay time δ =24h.

The elements Ti, Mn, V, and Al are treated as impurities in the Si-Mag-Sm sample, and their impacts were consequently discarded because of their physical characteristics, such as half-life and shock sections considerably lower than those of $^{152}Sm$. The activity calculation results suggest that the other elements in the sample would not present radioactive activity greater than $^{153}Sm$ after 24 hours, implying that samarium is radioactively interesting for the purposes of this study.

In order to evaluate the application potential for these nanoparticles, the magnetic heating behavior of Si-Mag and Si-Mag-

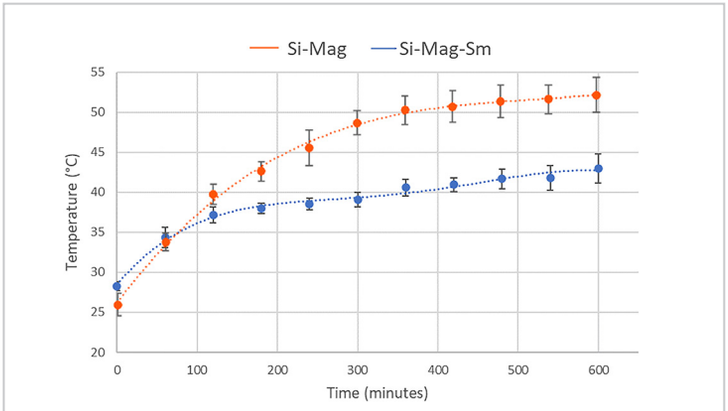


Figure 8 - Heating profiles of Si-Mag and Si-Mag-Sm exposed to AC magnetic field (amplitude: 30 $kAm^{-1}$; frequency: 356 kHz).

Sm was determined via AMF (amplitude: 30 $kAm^{-1}$; frequency: 356 kHz); the resulting heating profiles are presented in Figure 8.

For effective therapeutic applications involving hyperthermia, the cancerous tissue must reach 42–45 °C. As seen in Figure 8, the results for both samples were within this range: when the samples were exposed to AMF for 10 min, the temperature increased from 27 °C to approximately 50°C and 43°C for Si-Mag and Si-Mag-Sm, respectively. These results indicate that both samples offer promise for such therapeutic applications.

## 4. Conclusion

The natural iron oxide nanoparticles were confirmed to contain mostly natural magnetite ($Fe_3O_4$), and further investigation confirmed the presence of two other minority phases, maghemite ($\gamma$-$Fe_2O_3$) and hematite ($\alpha$-$Fe_2O_3$), as well as traces of other oxides (6%). The magnetic and morphological properties of these nanoparticles indicate that they may be well suited as agents for therapies involving magnetic hyperthermia.

In this initial study, developed nanocomposites with a core-shell structure formed from natural iron oxide nanoparticles were processed using the modified Stöber method and incorporating silica and samarium (Si-Mag-Sm) for potential application in combined cancer therapies involving hyperthermia and brachytherapy. Formation of the particles containing silica, iron oxide, and samarium was confirmed via FTIR, XRD, and XRF: the Si-Mag-Sm sample contained 51% Fe and 5.1% Sm, and the Si-Mag sample contained 88% Fe. The lower content of Fe in the Si-Mag-Sm sample compared to the Si-Mag sample was an unexpected finding, and requires further investigation. The heat generated by the Si-Mag and Si-Mag-Sm samples when exposed to an alternating magnetic field, increased the temperature of the medium to 45 °C, sufficient to induce hyperthermia. Future studies should investigate the biological and therapeutic behavior of these nanoparticles, as well as the influence of natural iron oxide incorporated with silica and samarium in the treatment of cancer. Observation of performance in magnetic hyperthermia treatment as well as analyses of the thermal and chemical stability of these samples after heating are also necessary.

The theoretical dosimetric study showed that the most relevant radioactive element for the purposes of this study is samarium. Future research will subject the Si-Mag-Sm sample to neutron activation in order to prove the presence of $^{153}Sm$, the only element in the sample with potential for brachytherapy application, and to rule out the possibility that the other elements present have significant emissions capable of influencing treatment when irradiated. In medical applications, brachytherapy agents synthesized from $^{152}Sm$ will require less activation time (neutron bombardment) to obtain the same activity compared to conventional procedures that use other radionuclides. This, in turn, will make this process accessible to institutions that lack nuclear reactors but have sealed neutron sources, which generally have lower neutron fluxes than nuclear reactors.

## Acknowledgments

The authors wish to thank CEFET-MG for scholarship funding during the study period, the Center for Development of Nuclear Technology (CDTN), and the Leibniz Institute for New Materials (INM) in Saarbrücken, Germany for laboratory support to conduct this research. Our thanks also to CNPq, CAPES, and FAPEMIG (Project REMETTEC) for financial support and acquisition of equipment and supplies for this study. We also thank Gabriela Moreira Lana, M.Sc., Dr. Peter Oliveira (INM), Dr. José Domingos Ardisson, and Dr. Luis Fernandez-Outon (CDTN) for performing the sample characterization tests. Finally, thanks to Dr. Fernando Lameiras (CDTN) for providing the samarium nitrate used in this study.

## References

ALLAF, M. Athari; SHAHRIARI, M.; SOHRABPOUR, M. Monte Carlo source simulation technique for solution of interference reactions in INAA experiments: a preliminary report. ***Radiation Physics and Chemistry***, v. 69, n. 6, p. 461-465, Apr. 2004.

CEMBER, H. ***Introduction to health physics***. New York: Pergamon Press, 1987.

CEMBER, H.; JOHNSON, T. E. ***Introduction to health physics***. New York: Mcgraw-Hill Medical, 2009.

CHANÉAC, C.; TRONC, E.; JOLIVET, J. P. Magnetic iron oxide–silica nanocomposites. Synthesis and characterization. ***J Mater Chem***. v. 6, n. 12, p. 1905-1911, 1996.

CHILTON, A. B.; FAW, R. E.; SHULTIS, J. K. ***Principles of radiation shielding***. Englewood Cliffs: Prentice-Hall, 1984.

DEEPA, A. V.; PRIYA, M.; SURESH, S. Influence of samarium oxide ions on structural and optical properties of borate glasses. ***Scientific Research and Essays***. v. 11, n. 5, p. 57-63, 2016, 15 Mar. 2016.

DELPINO, G. P.; BORGES, R.; ZAMBANINI, T.; JOCA, J. F. S.; GAUBEUR, I.; SOUZA, A. C. S. *et al.* Sol-gel-derived 58S bioactive glass containing holmium aiming brachytherapy applications: a dissolution, bioactivity, and cytotoxicity study. ***Materials Science and Engineering,*** 119:111595, Feb. 2021.

DÖNMEZ, Ç. E. D.; MANNA, P. K.; NICKEL, R.; AKTÜRK, S.; VAN LIEROP, J. Comparative heating efficiency of cobalt-, manganese-, and nickel-ferrite nanoparticles for a hyperthermia agent in biomedicines. ***ACS Applied Materials & Interfaces***. v. 11, n. 7, p. 6858-6866, 24 Jan. 2019.

EBELMEN, M. Recherches sur les combinaisons des acides borique et silicique avec les éthers. ***Ann. Chimie Phys,*** v. 16, n. 25, p. 129-166, 1846.

FERRARO, J. R. The nitrate symmetry in metallic nitrates. ***Journal of Molecular Spectroscopy***. v. 4, n. 1-6, p. 99-105, Jan. 1960.

FERREIRA, R. V. ***Síntese e caracterização de nanopartículas magnéticas funcionalizadas com núcleo magnético***

***de magnetita***. 2008. Dissertação (Mestrado em Química) - Departamento de Química - Universidade Federal de Minas Gerais, Belo Horizonte, 2009.

GILCHRIST, R. K.; MEDAL, R.; SHOREY, W. D.; HANSELMAN, R. C.; PARROTT, J. C.; TAYLOR, C. B. Selective inductive heating of lymph nodes. ***Annals of Surgery,*** v. 146, n. 4, p. 596-606, Oct. 1957.

HWA, L.; HWANG, S. L.; LIU, L. C. Infrared and raman spectra of calcium alumino–silicate glasses. ***Journal of Non-Crystalline Solids,*** v. 238, n. 3, p.193-197, Sept. 1998.

INTERNATIONAL AGENCY FOR RESEARCH ON CANCER - IARC. ***World cancer report***: cancer research for cancer prevention. Geneva: World Health Organization, 2020. License: CC BY-NC-ND 3.0 IGO.

INSTITUTO NACIONAL DO CÂNCER - INCA. ***Câncer***: estadiamento. Rio de Janeiro, SD. Disponível em: < https://www.inca.gov.br/estadiamento/>. Acesso em: 12 nov. 2021.

LANA, G. M. ***Aplicação de partículas magnéticas revestidas com fosfatos de cálcio para tratamento de câncer de ovário.*** Dissertação (Mestrado em Engenharia de Materiais) - Centro Federal de Educação Tecnológica de Minas Gerais. 2018.

MAHMOUDI, M.; SANT, S.; WAMG, B.; LAURENT, S.; SEN, T. Superparamagnetic iron oxide nanoparticles (SPIONs): development, surface modification and applications in chemotherapy. ***Advanced Drug Delivery Reviews,*** v. 63, n. 1-2, p. 24-46, Jan. 2011.

MOREIRA, G. F.; PEÇANHA, E. R.; MONTE, M. B. M.; LEAL FILHO, L. S.; STAVALE, F. XPS study on the mechanism of starch-hematite surface chemical complexation. ***Minerals Engineering,*** n. 110, p. 96-103, Aug. 2017.

PARETA, R. A.; SIRIVISOOT, S. Calcium phosphate-coated magnetic nanoparticles for treating bone diseases. ***Nanomedicine,*** p. 131-48, 2012.

ROBERTO, W. S.; PEREIRA, M. M.; CAMPOS, T. P. R. Structure and dosimetric analysis of biodegradable glasses for prostate cancer treatment. ***Artificial Organs,*** v. 27, n. 5, p. 432-436, 9 May 2003.

RUBIO, F.; RUBIO, J.; OTEO, J. L. A FT-IR study of the hydrolysis of tetraethylorthosilicate (TEOS). ***Spectroscopy Letters,*** v. 31, n. 1, p. 199-219. Jan. 1998.

STÖBER, W.; FINK, A.; BOHN, E. Controlled growth of monodisperse silica spheres in the micron size range. ***Journal of Colloid and Interface Science,*** v. 26, n. 1, p. 62-69, Jan. 1968.

VRATNY, F.; KOKALAS, J. J. The reflectance spectra of metallic oxides in the 300 to 1000 millimicron region. ***Applied Spectroscopy,*** v. 16, n. 6, p. 176-184, Jun. 1962.

WANG, Y.; MURAMATSU, A.; SUGIMOTO, T. FTIR analysis of well-defined $\alpha$-$Fe_2O_3$ particles. ***Colloids and Surfaces A: Physicochemical and Engineering Aspects,*** v. 134, n. 3, p. 281-297, Mar. 1998.

WORLD HEALTH ORGANIZATION. ***WHO report on cancer***: setting priorities, investing wisely and providing care for all. Geneva: World Health Organization; 2020. License: CC BY-NC-SA 3.0 IGO.

WRIGHT, J. D.; SOMMERDIJK, N. A. J. M. ***Sol-Gel materials.*** CRC Press, 2018.

Received: 14 September 2022 - Accepted: 3 February 2023.